

A versatile Johansson-type tender x-ray emission spectrometer

HPSTAR
917-2020

Cite as: Rev. Sci. Instrum. 91, 033101 (2020); doi: 10.1063/1.5121853

Submitted: 19 August 2019 • Accepted: 13 February 2020 •

Published Online: 3 March 2020



View Online



Export Citation



CrossMark

S. H. Nowak,¹  R. Armenta,¹ C. P. Schwartz,¹  A. Gallo,¹ B. Abraham,¹ A. T. Garcia-Esparza,¹  E. Biasin,¹ A. Prado,¹ A. Maciel,¹ D. Zhang,¹ D. Day,¹ S. Christensen,² T. Kroll,¹ R. Alonso-Mori,¹ D. Nordlund,¹ T.-C. Weng,^{1,3} and D. Sokaras^{1,a)} 

AFFILIATIONS

¹SLAC National Accelerator Laboratory, 2575 Sand Hill Rd., Menlo Park, California 94025, USA

²National Renewable Energy Laboratory, 15013 Denver West Parkway, Golden, Colorado 80401, USA

³Center of High Pressure Science and Technology Advanced Research (HPSTAR), Shanghai 202103, China

^{a)}Author to whom correspondence should be addressed: dsokaras@slac.stanford.edu

ABSTRACT

We present a high energy resolution x-ray spectrometer for the tender x-ray regime (1.6–5.0 keV) that was designed and operated at Stanford Synchrotron Radiation Lightsource. The instrument is developed on a Rowland geometry (500 mm of radius) using cylindrically bent Johansson analyzers and a position sensitive detector. By placing the sample inside the Rowland circle, the spectrometer operates in an energy-dispersive mode with a subnatural line-width energy resolution (~ 0.32 eV at 2400 eV), even when an extended incident x-ray beam is used across a wide range of diffraction angles ($\sim 30^\circ$ to 65°). The spectrometer is enclosed in a vacuum chamber, and a sample chamber with independent ambient conditions is introduced to enable a versatile and fast-access sample environment (e.g., solid/gas/liquid samples, *in situ* cells, and radioactive materials). The design, capabilities, and performance are presented and discussed.

Published under license by AIP Publishing. <https://doi.org/10.1063/1.5121853>

I. INTRODUCTION

The broad availability of synchrotron radiation facilities has established high energy resolution x-ray spectroscopy as a powerful characterization tool that provides element- and site-specific electronic structure insights. For example, x-ray emission (XES), resonant inelastic x-ray scattering (RIXS), and high energy resolution fluorescence detected x-ray absorption spectroscopy (HERFD-XAS) have been extensively used to give insights on energetics, momentum, and spin of transition metal oxides/complexes and superconductors, characterize *ex situ* and *in situ* catalytic reactions on surfaces and nanostructures,^{1–12} as well as to decipher the structure and role of metals in metalloenzymes.^{13–22} Moreover, the sub-50 fs temporal resolution of the Linear Coherent Light Source (LCLS),²³ SACLA,²⁴ European XFEL,²⁵ and several new x-ray free electron lasers provides the opportunity for these techniques to shed light on ultrafast dynamics,^{21,26–30} such as electron transfer processes, transient molecular states, and molecular dissociation, as well as to study radiation sensitive samples with the “probe-before-destroy” approach.^{26,31}

To adequately perform x-ray emission spectroscopy, some stringent requirements for both the detection energy resolution and the detection throughput should be met. Energy resolution should be comparable, and preferably superior, to the width of the core-levels, while the detection efficiency should be sufficient to permit meaningful measurements in reasonable acquisition times for a broad range of applications of interest. Accounting for a divergent emission source, i.e., the (quasi) isotropic emission from an irradiated sample, efficient detection schemes commonly employ curved diffraction x-ray optics across the whole range of x-ray energies.

In the soft x-ray regime (~ 0.2 – 1.2 keV), grating-based concepts on Rowland circles are usually incorporated.³² The long wavelength of soft x rays fulfills the diffraction condition with a reasonable reflectivity in shallow incident angles, resulting in solid angles of detection in the order of $\sim 10^{-4}$ of 4π while dictating demanding requirements for the effective incident beam size (few μm) to achieve resolving powers in the order of ~ 1000 .^{33,34} Advances in x-ray optics have led to elaborate concepts, including parabolic high-reflectivity variable line-spacing gratings and pre-mirror

implementations, which improve the throughput by more than an order of magnitude.^{35,36} Additionally, Transition Edge Sensor (TES) technology detectors are now rapidly evolving and have demonstrated a further throughput push of one to two orders of magnitude while maintaining a competitive energy resolution ($E/\Delta E \sim 500$) without any incident beam size restrictions.^{37–39} The ongoing progress on TES multi-pixelated detectors is expected to substantially impact soft x-ray spectroscopy in the following years.

In the hard x-ray regime (~ 5 – 20 keV), Bragg type perfect crystals are the backbone of high throughput and high energy resolution detection. Si and Ge bent crystals, usually of 0.5 – 1 m bent radius, are typically used in Johann (spherically bent) or Von Hamos (cylindrically bent) geometries,^{40,41} several high throughput instruments have been built on this basis with solid angles of detection of up to 1% and resolving powers that exceed 7000 .^{42–47} Von Hamos geometry is an energy-dispersive concept that simultaneously collects an extended energy spectrum on a position sensitive detector without moving/scanning parts. On the other hand, Johann is a point-to-point Rowland scanning geometry, i.e., at each point, the overall solid angle of the instrument is used to detect a very specific x-ray energy. Either of these Bragg optics based geometries operates optimally at close-to-backscattering angles ($\sim 70^\circ$ – 89°) because (i) beam size effects have a smaller contribution in the energy resolution, (ii) the effective solid angle (sr per detected eV) is higher, and (iii) the geometrical Johann aberrations (due to the size of the analyzers) are not prominent.^{42,43,48} A close-to-backscattering detection is feasible for practically any hard x-ray energy, by selecting a Bragg crystal analyzer with a proper d -spacing among a plethora of available Si/Ge cuts (see, for example, Fig. 7 in Ref. 43). However, when tender x-ray energies are of interest, the possible close-to-backscattering Si/Ge d -spacing options become very limited, since the sparsely available cuts [e.g., Si(111), Si(220), and SiO₂(10 $\bar{1}$ 0)] can diffract only a few narrow energy ranges within 2.0 – 4.5 keV at close-to-backscattering angles.

To overcome the aforementioned limitation, a versatile tender x-ray emission instrument has to either use analyzers based on other perfect Bragg crystal materials that have a finely tunable larger d -spacing⁴⁹ or find ways to operate efficiently with the commonly available Si/Ge cuts in a wider Bragg angle range away from backscattering. The latter has been demonstrated when adopting a modified Rowland geometry; when using a cylindrically bent analyzer, placing the sample inside the Rowland circle, and using a position sensitive detector, a spectrum can be recorded in an energy dispersive mode for a wide range of Bragg angles and with no prominent beam size influence.^{50–52} A further improvement of this concept replaces the simple cylindrically bent crystal with a Johannson analyzer, as demonstrated by Kavčič *et al.*^{53,54}

In this paper, we present a high energy resolution Johannson x-ray spectrometer that operates throughout the tender x-ray regime (1.6 – 5.0 keV) and was recently designed and operated at Stanford Synchrotron Radiation Lightsource. We discuss its basic concept through its characteristics and performance. As a main novelty, we emphasize the design and implementation of a sample chamber with independent ambient conditions, which enables the instrument to perform a broad range of applications.

II. SPECTROMETER CONCEPT AND DESIGN

The instrument developed targets x-ray emission spectroscopy across the entire tender x-ray regime (1.6 – 5.0 keV) for a broad range of scientific applications. Briefly, the spectrometer is designed in a Rowland geometry with cylindrical Johannson Bragg analyzers; their Bragg planes are bent to a 1000 mm radius and their optical surface ground to a 500 mm radius. An outline of the adopted configuration is shown with a Monte Carlo ray-tracing schematic in Fig. 1.

An exact Johannson geometry inherently waves the aberrations of the Johann concepts, even for Bragg angles away from backscattering. Hence, a point-to-point Rowland concept with Johannson analyzers is likely the most efficient way to perform high energy resolution tender x-ray emission spectroscopy with Si/Ge type of analyzers at low Bragg angles. However, in practice, this concept has two main difficulties: (a) The point-to-point Johannson geometry still suffers from the beam size energy resolution dependence, which becomes prominent when operating at low Bragg angles. For example, an incident beam of several hundred μm of size would result to an energy resolution that would limit the resonant spectroscopy studies like HERFD or RIXS [see formula (3) in Bergmann and Cramer⁴⁸]. (b) The fabrication of Johannson analyzers, which require a different bent radius for the Bragg planes and the optical surface, respectively, is significantly more challenging when

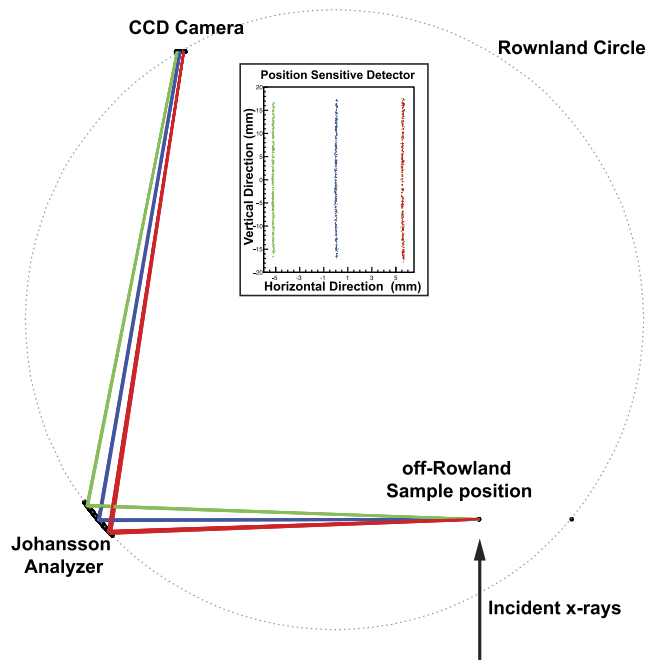


FIG. 1. A Monte Carlo ray-tracing top-view schematic of the adopted Johannson dispersive geometry. The off-Rowland sample position enables the energy dispersion when a position sensitive detector is used. In this ray-tracing, a Si(111) analyzer is set at a Bragg angle of 50° . Elastic scattering from a $1\text{ mm} \times 1\text{ mm}$ x-ray beam of 2565.9 eV (red) 2580.9 eV (blue), and 2595.9 eV (green) is diffracted by the represented areas of the cylindrically bent Johannson analyzer. The sample is positioned at 150 mm off the Rowland circle position. The inset presents the corresponding x-ray events on the surface of the position sensitive detector.

compared to simple curved Johann optics. Although the processing of Si/Ge has improved a lot over the years, achieving a homogeneous and precise ground along the analyzer extended area remains far from straightforward. In this way, analyzer surface imperfections can degrade the energy resolution performance of a point-to-point geometry that uses the overall surface of the x-ray optic to detect a specific x-ray energy.

In line with the previous work by Kavčič *et al.*,⁵⁴ the challenges above can be overcome by placing the sample off the Rowland circle. This offset allows an efficient collection of x rays from an extended emitting volume by using the overall incident photon flux of an incident beam of up to several mm (i.e., no need of slits to limit the x-ray source size). Since the source is now away from the ideal Rowland position, the Bragg angle along the analyzer's surface has a lateral dependence and, therefore, a corresponding energy dependence. When a position sensitive camera is used as a detector, an energy-dependent spatial discrimination can be achieved (see Fig. 1). The aforementioned approach allows an energy dispersive mode of operation while it suppresses the beam size influence on energy resolution, even for Bragg angles down to 30°.⁵⁴ As seen in the Monte Carlo ray-tracing in Fig. 1 this off-Rowland concept uses only a part of the crystal for the diffraction of a given x-ray energy (whereas in a point-to-point geometry, the overall x-ray optic is used to detect a very specific energy, within its energy resolution bandpass). For the study of x-ray emission lines or full RIXS maps, this efficiency limitation is partly compensated by the dispersive mode of operation: i.e., the spectrometer is detecting simultaneously all the emission patterns of interest. However, for HERFD-XAS type of studies, which solely use the peak intensity of a given x-ray emission line, such a dispersive setup is engaging a narrow part of the analyzer surface; hence, the efficiency limitation compared to a point-to-point geometry becomes more prominent. As discussed above though, when the beam size is large enough to hamper the energy resolution of resonant studies upon a point-to-point geometry, trading solid angle for energy resolution is certainly of an unprecedented value. Moreover, since in such dispersive mode, a given x-ray energy is diffracted only by a sub-part of the Johannsson analyzer, the influence of the overall analyzer inhomogeneities to the energy resolution is somewhat lessened (also, if a prominent artifact might be present on the analyzer's surface, this part could get directed to an energy region of no, or limited, interest).

A. Instrument

The spectrometer developed here is enclosed in an aluminum vacuum chamber of $1220 \times 965 \times 482 \text{ mm}^2$ (Fig. 2). For setting the spectrometer to a desired energy/Bragg angle, motorized stages can move the crystal analyzer and the detector to the appropriate Rowland circle positions. For the 500 mm Rowland circle radius geometry, the instrument operates within a Bragg angular range of 30°–65°. By selecting between three available analyzers [Quartz (10 $\bar{1}$ 0), Si(111), and Si(220)], x rays along the overall targeted tender x-ray regime can be analyzed [the size of the analyzers is 70 (h) \times 15 (v) mm²]. All crystals are pre-installed in the chamber, and a motorized stage can select the preferred crystal with no need of vacuum chamber access; this is an important practical feature since the instrument can be tuned within seconds to any energy within its overall attainable range. The spectrometer is set on the

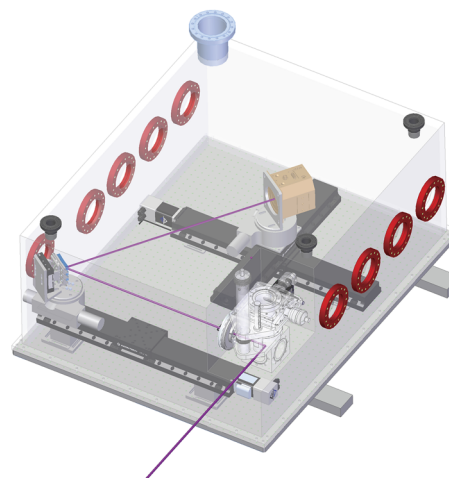


FIG. 2. A 3D technical model of the developed tender x-ray spectrometer. The incident and emitted x-ray beam paths are represented by the purple line.

polarization plane of the incident x-ray beam, and the analyzer is fixed at 90° with respect to the incident beam direction, minimizing the contribution of the non-resonant scattered radiation. A back-illuminated charge couple device camera (Andor DX436-BN CCD) is used as a position sensitive detector with >97% efficiency at 2 keV. This is an entire in-vacuum compatible camera consisting of 2048×2048 pixels of $13 \times 13 \mu\text{m}^2$ size. The camera chip is thermoelectrically cooled and typically operates at -60°C with the help of additional in-vacuum water cooling. At this temperature, the dark current is less than 1 electron/pixel/s. The camera is controlled by a Peripheral Component Interface (PCI) card and features a readout rate up to 1 MHz with a 32 bit analog to digital conversion protocol. A user-selected vertical binning can be selected for reducing the data readout dead time and the image file size.

The x-ray spectrometer was commissioned and operated at the 57-pole 0.9 T wiggler beamline 6-2a at SSRL. Beamline 6-2 is equipped with two liquid nitrogen cooled double crystal monochromators, a Si(111) ($\phi = 0$) and a Si(311) ($\phi = 0$) device that can be alternately used depending on the required energy resolution. For the tender x-ray range, only the Si(111) cut is used. A collimating and a focusing Rh-coated mirror are positioned (~ 3.5 mrad of incidence) before and after the monochromator, respectively. The beamline can operate over the range of 2.45–18 keV. For energies below 5 keV, the 3rd harmonic is minimized by 50% detuning of the monochromator. Under the current SPEAR3 storage ring operational conditions (electron energy of 3 GeV, current 500 mA in top-off mode), the Si(111) monochromator delivers an incident beam flux of $\sim 3 \times 10^{12}$ photons/s at 3.0 keV with an energy resolution of about 400 meV and a beam full width half maximum (FWHM) of about $400 \times 600 \mu\text{m}^2$ (v \times h) at the sample position (~ 26 m from the source). Typically, the sample is positioned 150 mm inside the Rowland circle. A 40 mm He ionization chamber is used for monitoring the incident flux, and a fast shutter is used to prevent sample illumination during the CCD readout.

B. Sample chamber

In order to enable a broad range of sample environments, the sample chamber is isolated from the main spectrometer vacuum chamber via a $13 \times 30 \text{ mm}^2$ opening covered with an $8 \text{ }\mu\text{m}$ polyimide film able to sustain an 1 atm pressure difference. This narrow opening also holds a collimating role, prohibiting most of the sample chamber diffused scattering/fluorescence from reaching the CCD camera. Since x-ray irradiated samples commonly experience x-ray luminescence, the polyimide film is coated with a $\sim 100 \text{ nm}$ of aluminum in order to prevent UV, visible, and infrared photons from reaching the CCD sensor. The sample chamber is air tight, and a continuous He flow is typically used to minimize the x-ray attenuation. This approach allows the implementation of *in situ* environments (e.g., liquid flow cells, *in situ* electrochemical cells, liquid jets, and gas reactors), radioactive samples, and other types of complex sample conditions because there are no ultra-high vacuum associated restrictions. At the same time, this concept allows immediate access for sample changes. A motorized XYZ stage is used to remotely drive the main sample rod. A magnetic mount based sample holder is attached to the sample rod tip permitting fast sample exchange and sample positioning with a high reproducibility. A 5 mm diameter photodiode is also mounted inside the sample chamber at a distance of $\sim 35 \text{ mm}$ from the sample; this facilitates the sample alignment process and also enables a Total Fluorescence Yield (TFY) x-ray absorption mode for the concentrated samples. Helium ionization chambers before and after the sample chamber are also incorporated.

III. DATA ACQUISITION AND SIGNAL PROCESSING

The instrument is controlled with an in-house developed software package built in MATLAB. This command line tool controls all spectrometer motors, the beamline optics/components, and the

data acquisition and also performs the online/offline data analysis. Briefly, this tool interconnects and supervises an Experimental Physics and Industrial Control System based motion control server that drives all spectrometer motorized stages, a C++ Andor Software Development Kit based server that controls the CCD, and the SPEC-based beamline control server. A 2D image analysis procedure has been developed to extract finalized x-ray spectra. A description of this procedure is presented further.

A typical CCD raw snapshot is presented in Fig. 3(a). Depicted is a 15 s recorded 2D digital raw image from a dibenzyl sulfide 100 mM liquid sample irradiated with incident photons of 3000 eV while the spectrometer is tuned at the sulfur- $K\alpha$ proximity. Each of the 2048×2048 pixels of the 2D image has assigned an analog-to-digital unit (ADU) proportional to the deposited energy. In line to the ray-tracing schematic presented in Fig. 1, the position sensitive detector is capturing an extended energy range along the horizontal direction (x-axis). Individual x-ray hits can be distinguished as bright spots. To ultimately extract a high-resolution energy dispersive spectrum, some intermediate analysis steps are required: first, the digital signal of the CCD has to be processed for isolating the intensity registered exclusively from x-ray photons, then the image has to be corrected for geometrical effects, and, ultimately, the 2D image needs to be projected along the energy dispersion axis.

A. CCD digital image processing

1. CCD signal

The histogram in Fig. 3(b) represents the ADU values of each pixel of the 2D exposure shown in Fig. 3(a). These ADU values are proportional to the deposited energy per pixel, and therefore, such a histogram resembles an energy dispersive spectrum of a solid state detector.^{55,56} The main characteristics of the histogram are (i) the intense baseline/background peak at ~ 885 ADU that corresponds to the pixels that have not received any deposited energy from x-ray

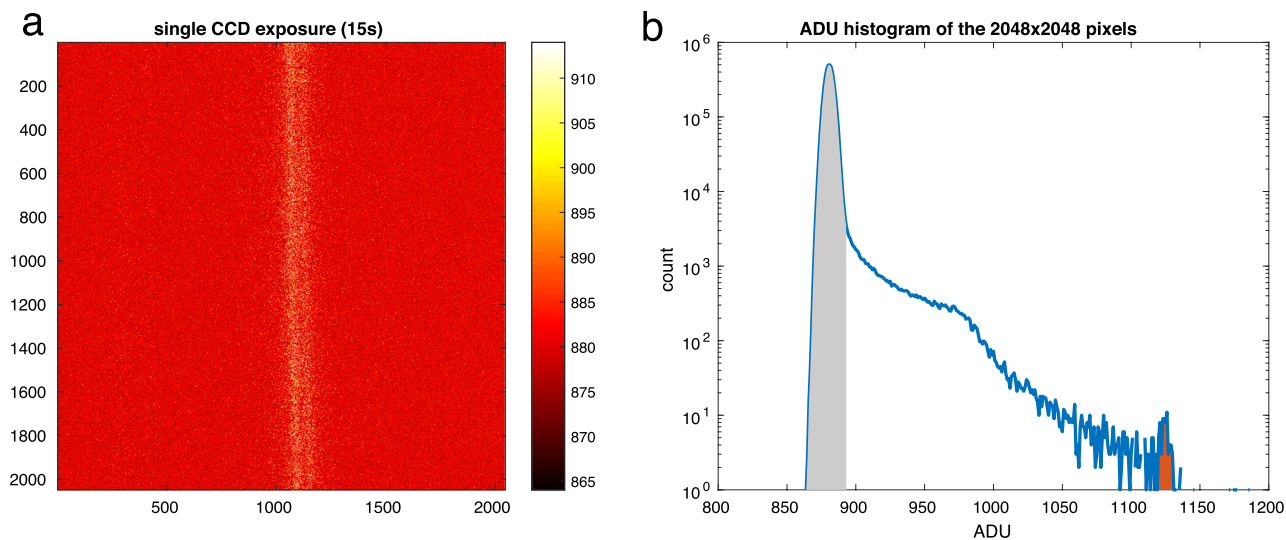


FIG. 3. (a) A raw CCD exposure of a 15 s S- $K\alpha$ measurement from a dibenzyl sulfide 100 mM liquid sample. (b) ADU histogram of the CCD pixels with baseline/background peak at ~ 885 ADU marked in gray and S- $K\alpha$ peak at ~ 1125 ADU marked in red.

photons, (ii) a weak peak at ~ 1125 ADU that corresponds to pixels that have registered the overall energy of S-K α photons, and (iii) a continuous distribution between the two aforementioned features that represents pixels where the S-K α photons deposited energy has been shared with their neighbors. In fact, the energy of an x-ray photon is deposited on a CCD silicon chip through a cascade of electron-hole pairs. Coulomb interactions and secondary collisions may expand the charge cloud up to tens of micrometer around the initial x-ray interaction point. Accounting the $13 \mu\text{m}^2$ pixel size of the CCD used here, most of the deposited energy of tender x rays can expand within an extended block of pixels around the x-ray interaction point.^{57,58}

Evidently, pixels with an appreciable amount of deposited energy are well-separated from the background peak. The isolation of pixels with a low deposited x-ray energy can be optimized with a reliable background peak reconstruction and by taking into account that the x-rays energy can be shared among neighboring pixels. It is important to emphasize again that here the term “background” refers to the ADU value registered for each pixel upon none x-ray photons energy deposition (not to be confused with any background contribution of x-ray origin). The background peak distribution has a width/noise that roughly represents the response (or the “energy resolution”) of the CCD pixels to a given deposited energy. The noise of the background value of each pixel (or the width of this background peak for all pixels) relates to the CCD dark current and the electronics readout noise. The dark current of the CCD can be minimized by cooling the camera (here down to -60°C) and by decreasing the acquisition time (in the order of a few seconds per frame).

A simple and direct method to reconstruct the background value of each pixel is to perform dark CCD exposures without the presence of x rays. To reliably reconstruct the background peak for a series of exposures, identical exposure conditions (acquisition time/camera temperature) are required for both the dark exposure frame and the frames of the actual measurements of interest.

Alternatively, the background response of each pixel can be extracted “on-the-fly” from a series of actual exposures with x rays by using a methodology that can reliably identify when pixels do not have registered any x-rays deposited energy. Such an approach, when applicable, could have a number of advantages since: (i) there is no need to consume time to periodically acquire dark frames, (ii) it can account for slow changes in the background upon long measurements, and (iii) it could remove any low energy deposited from UV/vis/IR photons that can origin, for example, from an intense x-ray luminescence (despite that here this component has been minimized with the Al coated window that separates the two chambers as described in Sec. II B).

2. On-the-fly CCD background extraction

The on-the-fly CCD background extraction approach developed here requires the following conditions: (1) an x-ray spectrum needs to be acquired in a series of sequential short exposures (frames), (2) the background conditions should not change significantly from one frame to another one, and (3) the x-ray photons need to be rare enough to permit each CCD pixel to record at least one background event (when accounting the exposure time per frame and the number of the overall frames). The analysis

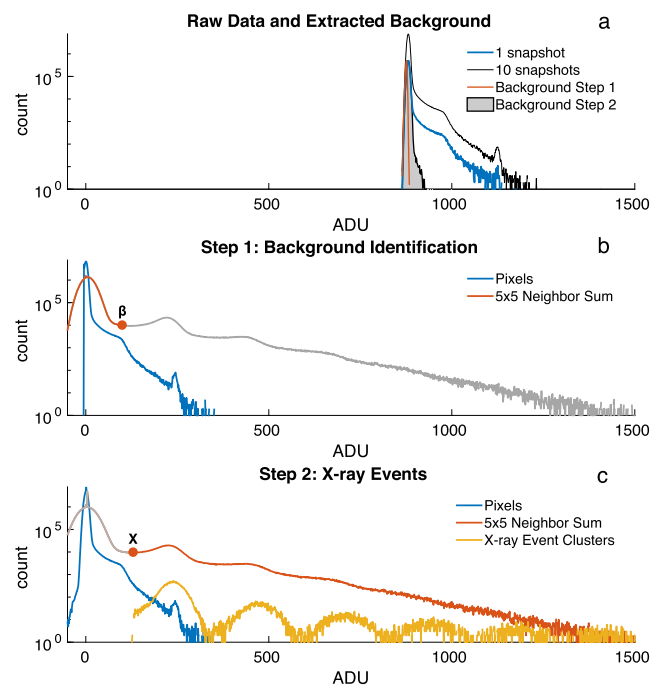


FIG. 4. An overview of the CCD signal processing steps. (a) ADU histograms for one and ten 15 s exposures from a S-K α measurement of a dibenzyl sulfide 100 mM liquid sample. The rough background estimated based on the minimal registered pixel value (Background Step 1, red trace) and the finalized optimized background response of the camera (Background Step 2, gray area) are shown. (b) The ADU histogram of the 10 exposures after subtraction of the “Background Step 1” (blue trace) and 5×5 pixels clustered intensity (red trace). Threshold β is also shown. (c) ADU histogram of the 10 exposures after subtraction of the finalized “Background Step 2” (blue trace) and 5×5 clustered intensity (red trace). Threshold X is also shown. A summarized histogram (yellow trace) of the isolated x-ray intensity events of 5×5 clusters (or disjointed clustered regions when 5×5 clusters partially overlap).

procedure will be described further using the example in Figs. 4(a)–4(c) that consists of 10 sequential exposures of 15 s (experimental conditions/sample are identical to the ones used for Fig. 3).

The first step of this approach aims to identify pixels that have registered *background events*. Initially, a first rough background response is estimated using the minimal registered signal of each pixel within the overall series of 10 exposures [Fig. 4(a), red trace]. This first underestimated background is subtracted from all frames [Fig. 4(b), blue trace]. Then, to account the sharing of the x-rays deposited energy among neighbor pixels, a simple re-clustering of pixels signal is performed [Fig. 4(b), red trace]. In this example, a 5×5 clustering is selected (i.e., the intensity of each pixel is replaced with the sum intensity of its 5×5 neighbors), which can re-capture more than 95% of the deposited energy and, therefore, can help distinguish the actual x-ray signal from the background peak. As a last step, when this clustered pixel intensity is below a user-predefined threshold [threshold β in Fig. 4(b)], then the central pixel of the 5×5 block is flagged as a *background event*. In this way, the pixel values that correspond to actual background level are flagged within the whole exposure series. It is worth noting that for tender x-ray

photons, a slightly smaller or larger clustering would also result in a similar performance, since the purpose of this step is not to recapture a single pixel all the x-ray deposited but to capture enough deposited energy so as to make clear the distinction between pixels with and without x-ray deposited signal.

Finally, to extract the optimized background response [Fig. 4(a), red trace] of each pixel, the median background value out of all its background flagged events is extracted (most commonly, for each pixel, there are several background flagged events within the exposure series). In case a pixel has not an identified *background event* within the series, then its background level is interpolated from the nearest *background event*-flagged neighbors. This final background image is ultimately subtracted from each original frame of the series [Fig. 4(c), blue trace].

3. X-ray events

Once the CCD background has been subtracted (either through the procedure described above or through a simple dark exposure), the next analysis step aims to identify and isolate the pixels with an actual x-ray photons deposited signal. The ultimate goal is to exclude (i.e., set to zero intensity) any pixels with non-x-rays deposited energy in order to remove their dark current noise contribution in the finalized x-ray spectrum. Similar to the procedure followed in the section above, a 5×5 clustering of the background subtracted raw data can recapture most of the x-ray deposited energy that has been shared among neighbor pixels [Fig. 4(c), red trace]. When this clustered intensity is more than a user predefined threshold [threshold X in Fig. 4(c)], then the central pixel is identified as an *x-ray event*. If the central pixel has an intensity of less than 25% of the threshold then it is excluded; this ensures the exclusion of pixels that might be located between two closely separate x-ray events and end up exceeding the threshold X due to the applied clustering. Then, the intensity of all but the flagged *x-ray events* and their 5×5 neighbors is set to 0.

Based on all these steps above, a finalized x-ray signal 2D image [Fig. 5(a)] is produced, which has exclusively the contributions of the background corrected *x-ray events* and their 5×5 neighbors. This 2D image will be used to ultimately extract a high resolution x-ray spectrum. The improvement of this processed 2D image when compared to the initial raw CCD image [Fig. 3(a)] is evident.

For visualizing the energy pattern of the recorded *x-ray events*, the intensity of the x-ray-flagged pixels of each exposure, together with their 5×5 neighbors, is clustered as single intensity events into the histogram of Fig. 4(c) (yellow trace). Moreover, when 5×5 pixel

blocks partially overlap within the same frame/exposure, they are all joined together in a single event, resulting in what appears to be harmonic events. This visualization step is used solely for quality control purposes and confirmation of the x-ray photon energy pattern that ultimately makes it in the finalized 2D image.

4. Geometrical corrections

The flat side of the Johansson analyzer results in a slightly curved footprint. A direct vertical projection of the filtered and background-free image, without accounting for this geometrical correction, would deteriorate the energy resolution [Fig. 5(b), blue trace]. This curved footprint shape has a rather complex dependence with the position of the spectrometer elements and the Bragg angle. Here, a generic numerical procedure is used to correct for this. The shape of curvature is assessed by dividing vertically (y -axis) the CCD image into a variable number of horizontal sections (typically 20 sections). These sections, after integration along the y -direction, are used to calculate a correlation vector between the first and each of the consecutive sections. The geometrical offset/shift between these sections can be calculated as the shift of the correlation vector maximum peak position. These maxima positions are fitted with a third degree polynomial that is ultimately used for the correction of the 2D image curvature. The impact of the curved footprint correction in the extracted x-ray spectrum is depicted with a red trace in Fig. 5(b).

B. Energy calibration and repeatability

Energy calibration of the spectrometer is typically performed using the elastic scattering of the incident monochromatic beam. For a given position of the spectrometer, a series of elastic peak acquisitions are performed along the energy region of interest (nominally, few tens of eV around the emission line of interest). A quadratic function has been empirically found to represent well the pixel position vs energy for an energy range of up to couple tens of eV. An example of such calibration is shown in Fig. 6.

The sample position along the incident beam direction can sensitively affect the detected energy since it directly affects the actual Bragg angle on the fixed analyzer surface. To accurately compare the energy scale between different samples, a precise repeatable positioning is needed (\sim tens of micrometers). Here, this is mostly based on the magnetic kinematic mount of the sample rod. However, when dealing with samples that might have irregular shapes or when comparing samples measured with a completely different sample holder/environment, an acquisition of an elastic scattering

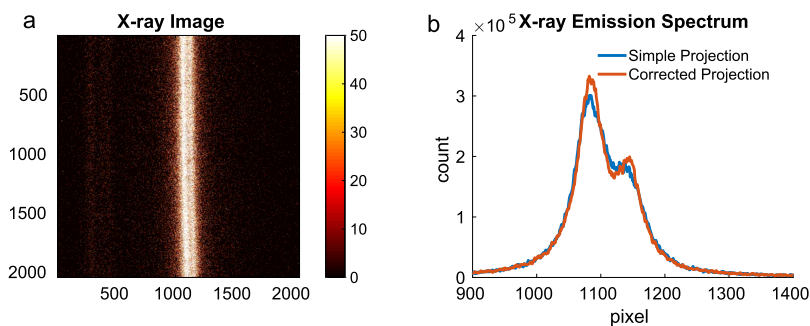


FIG. 5. (a) 2D CCD image based exclusively on the isolated x-ray events and upon subtraction of the estimated finalized background. (b) Final projected x-ray spectrum without and with geometrical correction of the curved x-ray footprint.

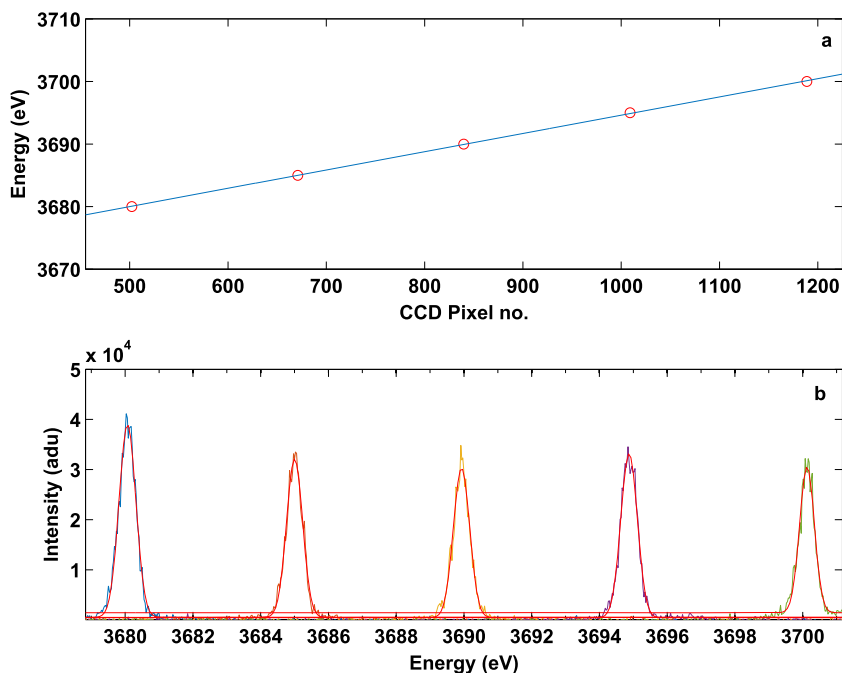


FIG. 6. An energy calibration example in the vicinity of the Ca- $K\alpha_{1,2}$ emission line [Si(220) analyzer]. A series of elastic scattering measurements (b) of the incident beam (3680.0, 3685.0, 3690.0, and 3695.0 eV) enables determination of the quadratic relationship between the CCD pixel number and the x-ray photon energy (a).

peak within the emission energy of interest is measured to correct any geometry-induced minor energy shifts with an accuracy down to tens of meV.

IV. PERFORMANCE AND APPLICATIONS

The spectrometer design and development approach aims to enable high energy resolution tender x-ray spectroscopy studies for a diverse range of applications by a careful consideration of detection throughput, energy resolution, accommodation of various sample environment conditions, and the easiness of changing the analyzed energy. The following subsections present the energy resolution of the instrument across a broad range of Bragg angles and energies, and representative examples from diverse sample environments/science cases so as to emphasize the capabilities of the instrument, the feasibility of the exemplary studies, and highlight the overall advantages of the high resolution tender x-ray spectroscopy toward new and unexplored fields of research.

A. Energy resolution

The spectrometer energy resolution consists of the Darwin width of the Bragg analyzer, the geometry effects related to the beam size and the camera pixel width (including charge sharing between pixels), as well as the accuracy of geometrical correction of the curved shape of the x-rays footprint. Here, the energy response has been assessed across a broad range of Bragg angles using the elastic scattering of the monochromatic incident radiation of the BL6-2 Si(111) monochromator. In Fig. 7, some representative elastic peaks are presented. The elastic scattering response is the superposition of the spectrometer [a Si(111) or Si(220), as indicated] and that of the Si(111) monochromator. After deconvoluting the

dynamical diffraction theory estimated broadening⁵⁹ of the incident beam ($FWHM_{mono}$), an approximate $FWHM_{spec}$ of the spectrometer response can be extracted ($FWHM_{spec} = \sqrt{FWHM^2 - FWHM_{mono}^2}$). It is worth noting that, in reality, the actual incident beam energy broadening can be larger than the dynamical theory estimation due to heat effects on the LN₂ cooled monochromator from the intense wiggler radiation (500 mA at SSRL), as well as due to a non-perfectly collimated white beam received by the monochromator. Furthermore, the pronounced angular dependence of the elastic scattering cross section of polarized x rays close to 90° leads to a non-homogeneous irradiation of the crystal surface and, therefore, can also have a minor impact. In summary, the estimated response of the spectrometer (shown in parentheses) when subtracting the monochromator theoretical contribution for the Si(111) analyzer values are 2460 eV (0.32 eV), 2840 eV (0.41 eV), 3165 eV (0.50 eV), 3520 eV (0.58 eV), and 3710 eV (0.76 eV) and for the Si(220) analyzer at 3685 eV (0.25 eV).

B. Examples of applications

The 4d transition metals are used extensively for catalysis applications. Their unpaired d electrons provide these elements with advantageous chemical characteristics while maintaining a high stability under harsh conditions. Elements such as Ru, Mo, Rh, and Pd are quite common building blocks for nanostructured heterogeneous catalysts and are typically studied under operating conditions through K near-edge and extended-range XAS. The dipole allowed $2p \rightarrow 4d$ transitions empower $L_{2,3}$ -XAS to be an ideal spectroscopic tool for near edge studies. However, the 4d elements' lifetime broadening (>2 eV) and the sample environment difficulties associated with their energies (when it comes to *in situ* measurements) have not permitted the extensive use of conventional L-edge XAS.

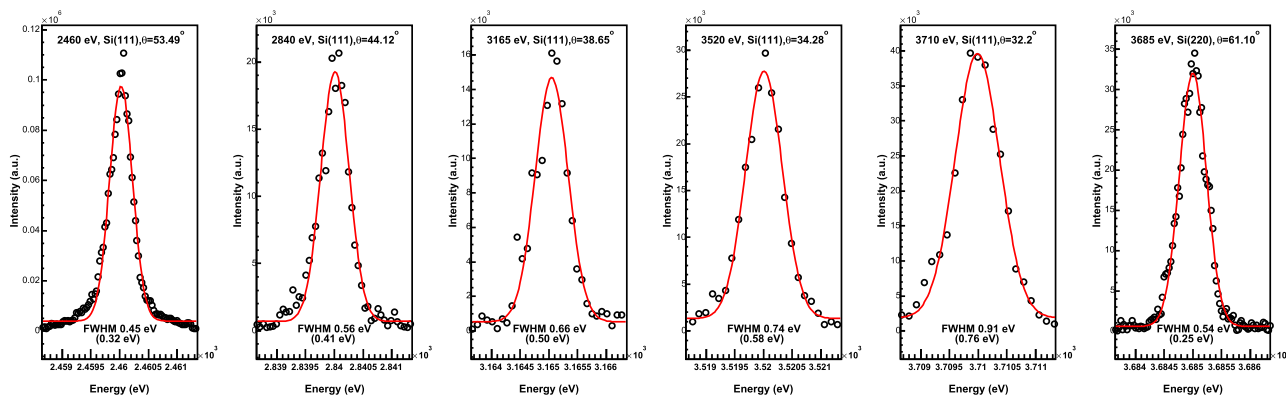


FIG. 7. A series of elastic scattering peaks across a broad range of Bragg angles/energies of the spectrometer. The fitted *FWHM* and the extracted estimation of the spectrometer contribution (in parentheses) are indicated. The analyzer and the Bragg angle for each case are shown at the top of each sub-figure.

Figure 8 shows an operando high energy resolution L_3 edge study of Pd ~ 2 nm nanoparticles loaded (2% concentration) on an Al_2O_3 support. This study has been realized by placing a fixed-bed (2 mm diameter) gas flow reactor with a $25 \mu\text{m}$ Kapton x ray in/out window inside the versatile sample chamber.⁶⁰ The operando data presented demonstrate the unique sensitivity of the Pd L_3 HERFD-XAS to Pd nanoparticles chemical changes, the complementary information that can be extracted for the occupied states by high energy resolution L_3 valence XES, and, ultimately, the feasibility with such an apparatus to efficiently perform gas phase heterogeneous catalysis studies on $4d$ elements L -edges under actual operating conditions and for concentrations relevant to catalysis research.

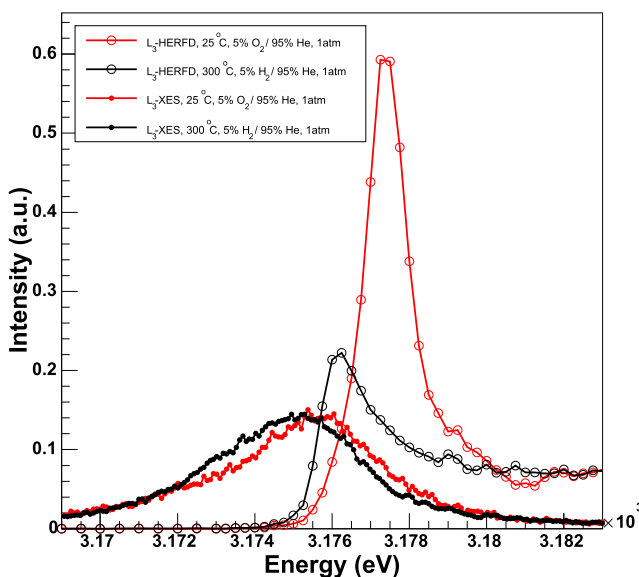


FIG. 8. Operando Pd L_3 HERFD and Pd L_3 -valence XES of ~ 2 nm Pd nanoparticles loaded with a 2% concentration on an alumina support. Non-resonant XES spectra (at 3250 eV incident energy) were acquired for 60 min each. The HERFD-XAS spectra required 20 s for each energy point.

Moreover, $4d$ metals have also earned a central role in photocatalysis and photochemistry applications. For example, Ru molecular complex based dyes have been shown to exhibit remarkable solar photoabsorption efficiency and have been incorporated in many model photocatalyst systems.^{61–64} X-ray spectroscopy studies can extract key insights on their electronic structure as well as their excited states dynamics with pump-probe approaches. In either way, such studies on molecular complexes often require quick sample replenishment due to radiation damage (static measurements) and/or the need for fresh sample (pump-probe). Therefore, liquid

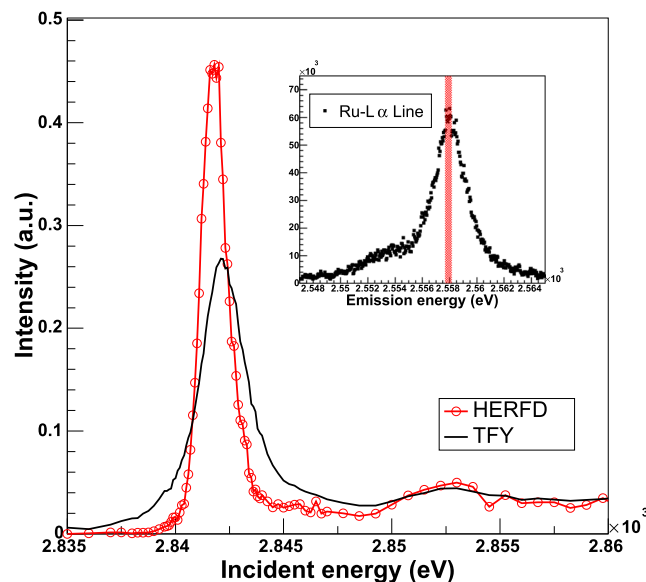


FIG. 9. A Ru- L_3 high energy resolution x-ray absorption spectrum of $\text{RuBpy}_2\text{Cl}_2$. A 5 mM concentrated aqueous $250 \mu\text{m}$ cylindrical jet. The inset shows the Ru $L_{\alpha,2}$ emission lines dispersively recorded with the tender x-ray spectrometer; the marked area represents the nine CCD bins integrated for every incident energy to ultimately extract the HERFD-XAS spectrum. Each incident energy point was measured for 40 s.

jet sample delivery approaches are mandatory to enable such measurements. In Fig. 9, the Ru L_3 HERFD-XAS of a 5 mMol RuBpy₂Cl₂ in a 250 μ m cylindrical jet pumped with a HPLC pump (\sim 5 ml/min) is demonstrated. For this, the versatile sample chamber accommodates a continuous flow liquid jet based on a Kapton capillary, while a catcher placed in the bottom of the chamber also allows a closed loop operation via fluid re-circulation. The inset in Fig. 9 presents the Ru- $L\alpha_{1,2}$ emission line that is dispersively recorded, while the shaded area represents the part of the emission line integrated for the extraction of the HERFD-XAS. This demonstrates the efficiency of the apparatus to enable the study of dilute transition metal complexes delivered with flowing liquid jets.

High energy resolution hard x-ray spectroscopy has extensively shown the rich information contained in the valence XES lines, accompanied by the rather simple and direct theoretical interpretation of such spectroscopic features through ground state density functional theory (DFT) calculations.³ Trying to capture similar fingerprints in the tender x-ray regime is of a great interest and value. The main limitations toward this goal are related to the very weak nature of these valence emission lines, as well as, in the case of 4d transition elements, for example, the core-hole lifetime broadening that can further limit the spectral details that can be resolved. The

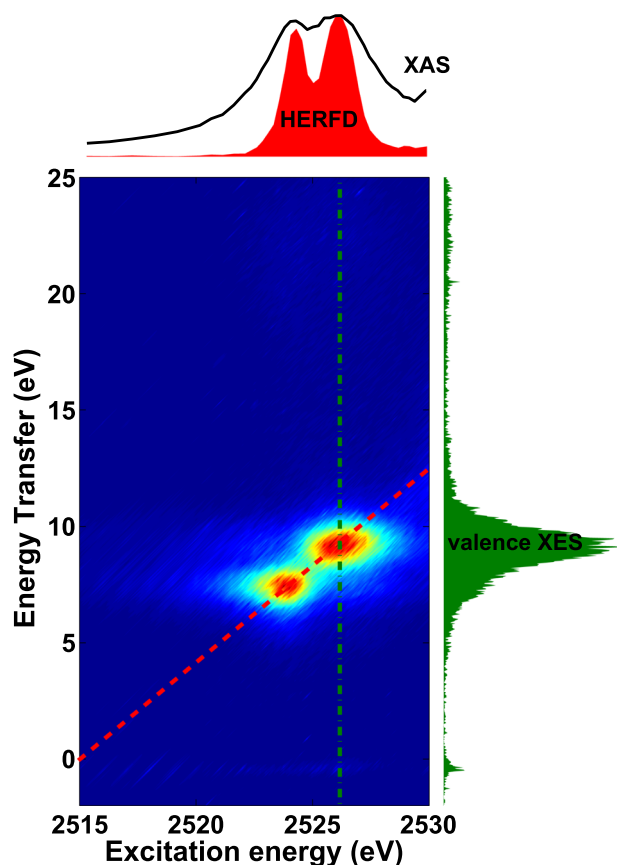


FIG. 10. Mo- L_3 valence RIXS of a bulk Na₂MoO₄ sample. Acquisition time of 2 min per incident energy.

most promising approach to overcome these difficulties is to move toward resonant valence XES since (a) the intense absorption resonances can significantly enhance the emission signal and (b) the core-hole broadening suppression can be advantageous for better resolving the spectral fingerprints. Nonetheless, resonant valence XES theoretical interpretations could become more challenging (when compared to ground state DFT) in order to account for the presence of excited core-electrons. The rapid progress and availability of advanced *ab initio* codes such as OCEAN⁶⁵ and ORCA⁶⁶ could, however, open the door to such applications for both molecular and extended solid state systems. In Fig. 10 is presented an overall Mo L_3 resonant valence XES map measured on a bulk Na₂MoO₄ sample demonstrating the capability of the apparatus to record reliably such weak emission lines. It is worth noting that performing measurements at 90° and on the polarization plane is rather critical for enabling resonant valence emission of dilute samples; otherwise, the Compton scattering contribution of the incident radiation would be the dominant contribution in the energy regime of the valence emission.

The very short lifetime of the actinides' core levels result in rather broad spectroscopic features (>5 eV) and, therefore, hamper the sensitivity of conventional x-ray spectroscopy. During the last 10 years, the advantage of the high energy resolution spectroscopy (HERFD/RIXS) has been used for the study of actinides L-edges.^{67,68} Recently, the potential of high energy resolution spectroscopy has been also shown for M -edges, which lie in the tender x-ray regime.^{69–71} In fact, the study of actinides' electronic structure through $M_{4,5}$ -edges allows the direct access of their partially filled f -states via the dipole allowed $3d \rightarrow 5f$ transitions. Consequently, instruments like the one presented here, i.e., that enable the access of all actinides edges and all their emission line energies, can now

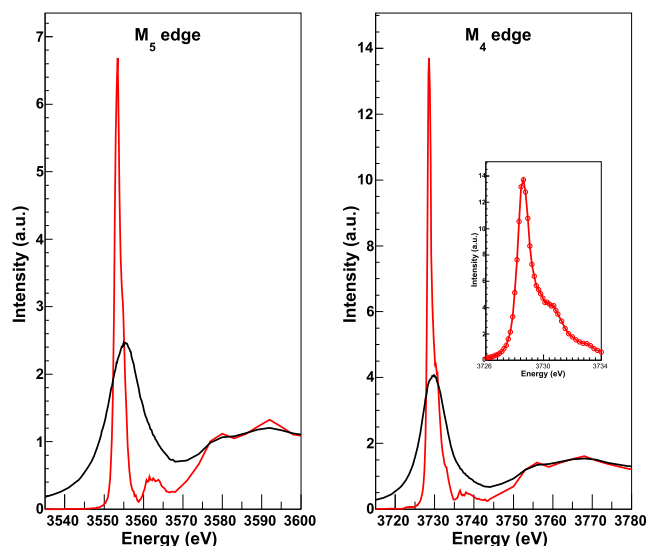


FIG. 11. High energy resolution x-ray absorption spectra for the M_4 and M_5 edges of a bulk UF₄ solid. [Reprinted with permission from Tobin *et al.*, J. Electron Spectrosc. Relat. Phenom. **232**, 100–104 (2018). Copyright 2018 Elsevier.] A comparison with the conventional x-ray absorption is also presented. Acquisition time of 20 s per energy point.

enable the study of this rather unexplored landscape and, ultimately, lead to novel insights for the $5f$ states localization and/or mixing in intermetallics and molecules. In Fig. 11 is presented the HERFD-XAS spectra of UF_4 measured at M_5 and M_4 edges via the $M\alpha$ and $M\beta$ emission lines, respectively (extracted from Tobin *et al.*⁶⁹). These high quality HERFD spectra from these materials were acquired with 20 s per energy point. It should be noted that based on safety procedures, actinides are commonly contained within protective layers (for the case of UF_4 , there was 75 μm of Kapton), which may attenuate significantly the tender x rays; therefore, high throughput detection can be necessary even for fairly concentrated actinide materials, especially when moving toward more radioactive hot specimens (Pu, Am, etc.).

V. CONCLUSION

High energy resolution x-ray spectroscopy in the tender x-ray regime can enable the study of key elements such as sulfur, chlorine, calcium, $4d$ transition metals, and $5f$ actinides through the strong symmetry-allowed dipole electronic transitions. A routine access to such characterization tools will provide new opportunities in the research of emerging catalysts, metalloproteins, and new materials developed for sustainable energy solutions. Moreover, since x rays in the tender x-ray regime are starting to become available at new x-ray free electron laser facilities such as LCLS-II⁷² and SwissFEL,⁷³ the development and availability of a high energy resolution apparatus becomes also central for the ultra-fast science community.

The main motivation of the instrument presented here is to enable and boost the systematic implementation of tender x-ray high energy resolution spectroscopy for a broad range of scientific applications. The developed spectrometer can provide subnatural line-width energy resolution spectra in the overall tender x-ray regime. The wide Bragg angle operation, the presence of all three crystal analyzers within the vacuum chamber, and the fully motorized motions allow changes to the detection energy within seconds. This is of great convenience when compared to close-to-back-scattering instruments that require crystal replacement and alignment efforts whenever a change of the detection energy is needed. Furthermore, as demonstrated, the design characteristics and overall performance of the apparatus can now enrich the research capabilities at SLAC to pursue tender x-ray spectroscopy static/operando studies in relevance to catalysis, chemistry/biochemistry, as well as actinide materials. The science program to be established with this capability will further expand and establish the role of high energy resolution x-ray spectroscopy.

ACKNOWLEDGMENTS

The spectrometer was funded by the U.S. Department of Energy, Office of Energy Efficiency and Renewable Energy, Solar Energy Technology Office BRIDGE Program. Parts of this work were performed at the Stanford Synchrotron Radiation Lightsource (SSRL) of the SLAC National Accelerator Laboratory; use of the SSRL was supported by the U.S. Department of Energy, Office of Basic Energy Sciences, under Contract No. DE-AC02-76SF00515. This study used resources of the National Energy Research Scientific Computing Center, a DOE Office of Science User Facility supported by the Office of Science of the U.S. Department of Energy under Contract No. DE-AC02-05CH11231. S.H.N. acknowledges financial

support by the Swiss National Science Foundation (SNSF), Project No. P2FRP2_148569.

REFERENCES

- 1 A. Kotani and S. Shin, "Resonant inelastic x-ray scattering spectra for electrons in solids," *Rev. Mod. Phys.* **73**, 203–246 (2001).
- 2 L. J. P. Ament, M. van Veenendaal, T. P. Devereaux, J. P. Hill, and J. van den Brink, "Resonant inelastic x-ray scattering studies of elementary excitations," *Rev. Mod. Phys.* **83**, 705–767 (2011).
- 3 P. Glatzel and U. Bergmann, "High resolution 1s core hole x-ray spectroscopy in 3d transition metal complexes—Electronic and structural information," *Coord. Chem. Rev.* **249**, 65–95 (2005), part of special issue on Synchrotron Radiation in Inorganic and Bioinorganic Chemistry.
- 4 U. Bergmann and P. Glatzel, "X-ray emission spectroscopy," *Photosynth. Res.* **102**, 255 (2009).
- 5 D. Friebe, M. W. Louie, M. Bajdich, K. E. Sanwald, Y. Cai, A. M. Wise, M.-J. Cheng, D. Sokaras, T.-C. Weng, R. Alonso-Mori, R. C. Davis, J. R. Bargar, J. K. Norskov, A. Nilsson, and A. T. Bell, "Identification of highly active Fe sites in (Ni, Fe)OOH for electrocatalytic water splitting," *J. Am. Chem. Soc.* **137**, 1305–1313 (2015).
- 6 C. Kuai, Y. Zhang, D. Wu, D. Sokaras, L. Mu, S. Spence, D. Nordlund, F. Lin, and X.-W. Du, "Fully oxidized Ni-Fe layered double hydroxide with 100% exposed active sites for catalyzing oxygen evolution reaction," *ACS Catal.* **9**, 6027–6032 (2019).
- 7 S. Sainio, N. Wester, C. J. Titus, Y. Liao, Q. Zhang, D. Nordlund, D. Sokaras, S.-j. Lee, K. D. Irwin, W. B. Doriese, G. C. O'Neil, D. S. Swetz, J. N. Ullom, E. I. Kauppinen, T. Laurila, and J. Koskinen, "Hybrid x-ray spectroscopy-based approach to acquire chemical and structural information of single-walled carbon nanotubes with superior sensitivity," *J. Phys. Chem. C* **123**, 6114–6120 (2019).
- 8 Y. Lu, J. Wang, L. Yu, L. Kovarik, X. Zhang, A. S. Hoffman, A. Gallo, S. R. Bare, D. Sokaras, T. Kroll *et al.*, "Identification of the active complex for CO oxidation over single-atom Ir-on-MgAl₂O₄ catalysts," *Nat. Catal.* **2**, 149 (2019).
- 9 L. Li, J. Yang, H. Ali-Loytty, T.-C. Weng, F. M. Toma, D. Sokaras, I. D. Sharp, and A. Nilsson, "Operando observation of chemical transformations of iridium oxide during photoelectrochemical water oxidation," *ACS Appl. Energy Mater.* **2**, 1371–1379 (2019).
- 10 L. R. Merte, F. Behafarid, D. J. Miller, D. Friebe, S. Cho, F. Mbuga, D. Sokaras, R. Alonso-Mori, T.-C. Weng, D. Nordlund, A. Nilsson, and B. Roldan Cuenya, "Electrochemical oxidation of size-selected Pt nanoparticles studied using *in situ* high-energy-resolution x-ray absorption spectroscopy," *ACS Catal.* **2**, 2371–2376 (2012).
- 11 J. J. Willis, A. Gallo, D. Sokaras, H. Aljama, S. H. Nowak, E. D. Goodman, L. Wu, C. J. Tassone, T. F. Jaramillo, F. Abild-Pedersen *et al.*, "Systematic structure–property relationship studies in palladium-catalyzed methane complete combustion," *ACS Catal.* **7**, 7810–7821 (2017).
- 12 A. T. Garcia-Esparza, T. Shinagawa, S. Ould-Chikh, M. Qureshi, X. Peng, N. Wei, D. H. Anjum, A. Clo, T.-C. Weng, D. Nordlund *et al.*, "An oxygen-insensitive hydrogen evolution catalyst coated by a molybdenum-based layer for overall water splitting," *Angew. Chem., Int. Ed.* **56**, 5780–5784 (2017).
- 13 U. Bergmann, P. Glatzel, and S. P. Cramer, "Bulk-sensitive XAS characterization of light elements: From x-ray Raman scattering to x-ray Raman spectroscopy," *Microchem. J.* **71**, 221–230 (2002), part of special issue on X-RAY ABSORPTION SPECTROSCOPY.
- 14 U. Bergmann, M. M. Grush, C. R. Horne, P. DeMarois, J. E. Penner-Hahn, C. F. Yocum, D. W. Wright, C. E. Dubé, W. H. Armstrong, G. Christou, H. J. Eppley, and S. P. Cramer, "Characterization of the Mn oxidation states in photosystem II by K β x-ray fluorescence spectroscopy," *J. Phys. Chem. B* **102**, 8350–8352 (1998).
- 15 U. Bergmann, C. Horne, T. Collins, J. Workman, and S. Cramer, "Chemical dependence of interatomic x-ray transition energies and intensities—A study of Mn K β ' and K $\beta_{2,5}$ spectra," *Chem. Phys. Lett.* **302**, 119–124 (1999).
- 16 K. M. Lancaster, M. Roemelt, P. Ettenhuber, Y. Hu, M. W. Ribbe, F. Neese, U. Bergmann, and S. DeBeer, "X-ray emission spectroscopy evidences a central carbon in the nitrogenase iron-molybdenum cofactor," *Science* **334**, 974–977 (2011).

- ¹⁷R. Alonso Mori, E. Paris, G. Giuli, S. G. Eeckhout, M. Kavčič, M. Žitnik, K. Bučar, L. G. M. Pettersson, and P. Glatzel, "Electronic structure of sulfur studied by x-ray absorption and emission spectroscopy," *Anal. Chem.* **81**, 6516–6525 (2009).
- ¹⁸R. A. Mori, E. Paris, G. Giuli, S. G. Eeckhout, M. Kavčič, M. Žitnik, K. Bučar, L. G. M. Pettersson, and P. Glatzel, "Sulfur-metal orbital hybridization in sulfur-bearing compounds studied by x-ray emission spectroscopy," *Inorg. Chem.* **49**, 6468–6473 (2010).
- ¹⁹P. Glatzel, J. Singh, K. O. Kvashnina, and J. A. van Bokhoven, "In situ characterization of the 5d density of states of Pt nanoparticles upon adsorption of CO," *J. Am. Chem. Soc.* **132**, 2555–2557 (2010).
- ²⁰T. Fransson, R. Chatterjee, F. D. Fuller, S. Gul, C. Weninger, D. Sokaras, T. Kroll, R. Alonso-Mori, U. Bergmann, J. Kern *et al.*, "X-ray emission spectroscopy as an *in situ* diagnostic tool for x-ray crystallography of metalloproteins using an x-ray free-electron laser," *Biochemistry* **57**, 4629–4637 (2018).
- ²¹M. W. Mara, R. G. Hadt, M. E. Reinhard, T. Kroll, H. Lim, R. W. Hartsock, R. Alonso-Mori, M. Chollet, J. M. Glownia, S. Nelson *et al.*, "Metalloprotein entatic control of ligand-metal bonds quantified by ultrafast x-ray spectroscopy," *Science* **356**, 1276–1280 (2017).
- ²²V. Martin-Diaconescu, K. N. Chacón, M. U. Delgado-Jaime, D. Sokaras, T.-C. Weng, S. DeBeer, and N. J. Blackburn, "K β valence to core x-ray emission studies of Cu(I) binding proteins with mixed methionine-histidine coordination. Relevance to the reactivity of the M- and H-sites of peptidylglycine monooxygenase," *Inorg. Chem.* **55**, 3431–3439 (2016).
- ²³P. Emma, R. Akre, J. Arthur, R. Bionta, C. Bostedt, J. Bozek, A. Brachmann, P. Bucksbaum, R. Coffee, F.-J. Decker *et al.*, "First lasing and operation of an ångstrom-wavelength free-electron laser," *Nat. Photonics* **4**, 641 (2010).
- ²⁴D. Pile, "X-rays: First light from SACLAs," *Nat. Photonics* **5**, 456 (2011).
- ²⁵M. Altarelli, R. Brinkmann, M. Chergui, W. Decking, B. Dobson, S. Düsterer, G. Grübel, W. Graeff, H. Graafsma, J. Hajdu *et al.*, "The European x-ray free-electron laser," in *Technical Design Report*, DESY 97 (2006), pp. 1–26, see <https://bib-pubdb1.desy.de/record/77248/files/european-xfel-tdr.pdf>.
- ²⁶R. Alonso-Mori, J. Kern, R. J. Gillea, D. Sokaras, T.-C. Weng, B. Lassalle-Kaiser, R. Tran, J. Hattne, H. Laksmono, J. Hellmich *et al.*, "Energy-dispersive x-ray emission spectroscopy using an x-ray free-electron laser in a shot-by-shot mode," *Proc. Natl. Acad. Sci. U. S. A.* **109**, 19103–19107 (2012).
- ²⁷R. Alonso-Mori, D. Sokaras, D. Zhu, T. Kroll, M. Chollet, Y. Feng, J. M. Glownia, J. Kern, H. T. Lemke, D. Nordlund *et al.*, "Photon-in photon-out hard x-ray spectroscopy at the LINAC Coherent Light Source," *J. Synchrotron Radiat.* **22**, 612–620 (2015).
- ²⁸W. Zhang, R. Alonso-Mori, U. Bergmann, C. Bressler, M. Chollet, A. Galler, W. Gawelda, R. G. Hadt, R. W. Hartsock, T. Kroll *et al.*, "Tracking excited-state charge and spin dynamics in iron coordination complexes," *Nature* **509**, 345 (2014).
- ²⁹K. S. Kjær, W. Zhang, R. Alonso-Mori, U. Bergmann, M. Chollet, R. G. Hadt, R. W. Hartsock, T. Harlang, T. Kroll, K. Kubiček *et al.*, "Ligand manipulation of charge transfer excited state relaxation and spin crossover in [Fe(2,2'-bipyridine)₂(CN)₂]," *Struct. Dyn.* **4**, 044030 (2017).
- ³⁰W. Zhang, K. S. Kjær, R. Alonso-Mori, U. Bergmann, M. Chollet, L. A. Fredin, R. G. Hadt, R. W. Hartsock, T. Harlang, T. Kroll *et al.*, "Manipulating charge transfer excited state relaxation and spin crossover in iron coordination complexes with ligand substitution," *Chem. Sci.* **8**, 515–523 (2017).
- ³¹J. Kern, R. Tran, R. Alonso-Mori, S. Koroidov, N. Echols, J. Hattne, M. Ibrahim, S. Gul, H. Laksmono, R. G. Sierra *et al.*, "Taking snapshots of photosynthetic water oxidation using femtosecond x-ray diffraction and spectroscopy," *Nat. Commun.* **5**, 4371 (2014).
- ³²J. Nordgren, G. Bray, S. Cramm, R. Nyholm, J.-E. Rubensson, and N. Wassdahl, "Soft x-ray emission spectroscopy using monochromatized synchrotron radiation," *Rev. Sci. Instrum.* **60**, 1690–1696 (1989).
- ³³K. Kunnus, I. Rajkovic, S. Schreck, W. Quevedo, S. Eckert, M. Beye, E. Suljoti, C. Weninger, C. Kalus, S. Grübel *et al.*, "A setup for resonant inelastic soft x-ray scattering on liquids at free electron laser light sources," *Rev. Sci. Instrum.* **83**, 123109 (2012).
- ³⁴Y.-D. Chuang, J. Pepper, W. McKinney, Z. Hussain, E. Gullikson, P. Batson, D. Qian, and M. Z. Hasan, "High-resolution soft x-ray emission spectrograph at advanced light source," *J. Phys. Chem. Solids* **66**, 2173–2178 (2005).
- ³⁵R. Qiao, Q. Li, Z. Zhuo, S. Sallis, O. Fuchs, M. Blum, L. Weinhardt, C. Heske, J. Pepper, M. Jones *et al.*, "High-efficiency *in situ* resonant inelastic x-ray scattering (iRIXS) endstation at the advanced light source," *Rev. Sci. Instrum.* **88**, 033106 (2017).
- ³⁶Z. Yin, J. Rehanek, H. Löchel, C. Braig, J. Buck, A. Firsov, J. Viehhaus, A. Erko, and S. Techert, "Highly efficient soft x-ray spectrometer based on a reflection zone plate for resonant inelastic x-ray scattering measurements," *Opt. Express* **25**, 10984–10996 (2017).
- ³⁷T. Jach, J. Terrence, R. Nicholas, U. Joel, and J. A. Beall, "Quantitative analysis with the transition edge sensor microcalorimeter x-ray detector," *Powder Diffr.* **22**, 138–141 (2007).
- ³⁸H. Tatsuno, W. B. Doriese, D. A. Bennett, C. Curceanu, J. W. Fowler, J. Gard, F. P. Gustafsson, T. Hashimoto, R. S. Hayano, J. P. Hays-Wehle *et al.*, "Absolute energy calibration of x-ray TESs with 0.04 eV uncertainty at 6.4 keV in a Hadron-Beam environment," *J. Low Temp. Phys.* **184**, 930–937 (2016).
- ³⁹C. J. Titus, M. L. Baker, S. J. Lee, H.-M. Cho, W. B. Doriese, J. W. Fowler, K. Gaffney, J. D. Gard, G. C. Hilton, C. Kenney *et al.*, "L-edge spectroscopy of dilute, radiation-sensitive systems using a transition-edge-sensor array," *J. Chem. Phys.* **147**, 214201 (2017).
- ⁴⁰H. H. Johann, "Die erzeugung lichtstarker Röntgenspektren mit Hilfe von Konkavkristallen," *Z. Phys.* **69**, 185–206 (1931).
- ⁴¹L. v. Hámos, "Röntgenspektroskopie und abbildung mittels gekrümmter kristallreflektoren," *Naturwissenschaften* **20**, 705–706 (1932).
- ⁴²R. Alonso-Mori, J. Kern, D. Sokaras, T.-C. Weng, D. Nordlund, R. Tran, P. Montanez, J. Delor, V. K. Yachandra, J. Yano *et al.*, "A multi-crystal wavelength dispersive x-ray spectrometer," *Rev. Sci. Instrum.* **83**, 073114 (2012).
- ⁴³D. Sokaras, T.-C. Weng, D. Nordlund, R. Alonso-Mori, P. Velikov, D. Wenger, A. Garachtchenko, M. George, V. Borzenets, B. Johnson, T. Rabedeau, and U. Bergmann, "A seven-crystal Johann-type hard x-ray spectrometer at the Stanford Synchrotron Radiation Lightsource," *Rev. Sci. Instrum.* **84**, 053102 (2013).
- ⁴⁴D. Sokaras, D. Nordlund, T.-C. Weng, R. A. Mori, P. Velikov, D. Wenger, A. Garachtchenko, M. George, V. Borzenets, B. Johnson *et al.*, "A high resolution and large solid angle x-ray Raman spectroscopy end-station at the Stanford Synchrotron Radiation Lightsource," *Rev. Sci. Instrum.* **83**, 043112 (2012).
- ⁴⁵E. Kleymenov, J. A. van Bokhoven, C. David, P. Glatzel, M. Janousch, R. Alonso-Mori, M. Studer, M. Willmann, A. Bergamaschi, B. Henrich *et al.*, "Five-element Johann-type x-ray emission spectrometer with a single-photon-counting pixel detector," *Rev. Sci. Instrum.* **82**, 065107 (2011).
- ⁴⁶J. Ablett, D. Prieur, D. Céolin, B. Lassalle-Kaiser, B. Lebert, M. Sauvage, T. Moreno, S. Bac, V. Balédent, A. Ovono *et al.*, "The galaxies inelastic hard x-ray scattering end-station at synchrotron soleil," *J. Synchrotron Radiat.* **26**, 263–271 (2019).
- ⁴⁷M. Moretti Sala, K. Martel, C. Henriquet, A. Al Zein, L. Simonelli, C. Sahle, H. Gonzalez, M.-C. Lagier, C. Ponchut, S. Huotari *et al.*, "A high-energy-resolution resonant inelastic x-ray scattering spectrometer at ID20 of the European Synchrotron Radiation Facility," *J. Synchrotron Radiat.* **25**, 580–591 (2018).
- ⁴⁸U. Bergmann and S. P. Cramer, "High-resolution large-acceptance analyzer for x-ray fluorescence and Raman spectroscopy," in *Crystal and Multilayer Optics* (International Society for Optics and Photonics, 1998), Vol. 3448, pp. 198–210.
- ⁴⁹B. Abraham, S. Nowak, C. Weninger, R. Armenta, J. Defever, D. Day, G. Carini, K. Nakahara, A. Gallo, S. Nelson, D. Nordlund, T. Kroll, M. S. Hunter, T. van Driel, D. Zhu, T.-C. Weng, R. Alonso-Mori, and D. Sokaras, "A high-throughput energy-dispersive tender X-ray spectrometer for shot-to-shot sulfur measurements," *J. Synchrotron Radiat.* **26**, 629–634 (2019).
- ⁵⁰E. Welter, P. Machek, G. Dräger, U. Brüggemann, and M. Fröba, "A new x-ray spectrometer with large focusing crystal analyzer," *J. Synchrotron Radiat.* **12**, 448–454 (2005).
- ⁵¹A. Hudson, W. C. Stolte, D. W. Lindle, and R. Guillemin, "Design and performance of a curved-crystal x-ray emission spectrometer," *Rev. Sci. Instrum.* **78**, 053101 (2007).
- ⁵²L. Journal, L. El Khoury, T. Marin, R. Guillemin, S. Carniato, A. Avila, R. Delaunay, C. F. Hague, and M. Simon, "Performances of a bent-crystal spectrometer adapted to resonant x-ray emission measurements on gas-phase samples," *Rev. Sci. Instrum.* **80**, 093105 (2009).
- ⁵³T. Johansson, "Über ein neuartiges, genau fokussierendes röntgenspektrometer," *Z. Phys.* **82**, 507–528 (1933).

- ⁵⁴M. Kavčič, M. Budnar, A. Mühleisen, F. Gasser, M. Žitnik, K. Bučar, and R. Bohinc, "Design and performance of a versatile curved-crystal spectrometer for high-resolution spectroscopy in the tender x-ray range," *Rev. Sci. Instrum.* **83**, 033113 (2012).
- ⁵⁵F. P. Romano, C. Caliri, P. Nicotra, S. Di Martino, L. Pappalardo, F. Rizzo, and H. C. Santos, "Real-time elemental imaging of large dimension paintings with a novel mobile macro x-ray fluorescence (MA-XRF) scanning technique," *J. Anal. At. Spectrom.* **32**, 773–781 (2017).
- ⁵⁶F. P. Romano, C. Caliri, L. Cosentino, S. Gammino, D. Mascali, L. Pappalardo, F. Rizzo, O. Scharf, and H. C. Santos, "Micro x-ray fluorescence imaging in a tabletop full field-x-ray fluorescence instrument and in a full field-particle induced x-ray emission end station," *Anal. Chem.* **88**, 9873–9880 (2016).
- ⁵⁷E. Miyata, M. Miki, D. Kamiyama, H. Tsunemi, and K. Miyaguchi, "Measurement of the charge cloud shape generated in the fully depleted back-illuminated charge-coupled device," *Jpn. J. Appl. Phys.* **42**, 7135–7139 (2003), single size component in fully depleted cloud.
- ⁵⁸S. H. Nowak, A. Bjeoumikhov, J. von Borany, J. Buchriegler, F. Munnik, M. Petric, M. Radtke, A. D. Renno, U. Reinholz, O. Scharf *et al.*, "Sub-pixel resolution with a color x-ray camera," *J. Anal. At. Spectrom.* **30**, 1890–1897 (2015).
- ⁵⁹J. Als-Nielsen and D. McMorrow, *Elements of Modern X-Ray Physics* (John Wiley & Sons, 2011).
- ⁶⁰A. Gallo, "A fixed-bed reactor for operando tender x-ray spectroscopy studies" (unpublished).
- ⁶¹T.-V. Nguyen, J. C. Wu, and C.-H. Chiou, "Photoreduction of CO₂ over ruthenium dye-sensitized TiO₂-based catalysts under concentrated natural sunlight," *Catal. Commun.* **9**, 2073–2076 (2008).
- ⁶²K. Maeda, G. Sahara, M. Eguchi, and O. Ishitani, "Hybrids of a ruthenium(II) polypyridyl complex and a metal oxide nanosheet for dye-sensitized hydrogen evolution with visible light: Effects of the energy structure on photocatalytic activity," *Acs Catal.* **5**, 1700–1707 (2015).
- ⁶³X. Zhang, G. Smolentsev, J. Guo, K. Attenkofer, C. Kurtz, G. Jennings, J. V. Lockard, A. B. Stickrath, and L. X. Chen, "Visualizing interfacial charge transfer in Ru-dye-sensitized TiO₂ nanoparticles using x-ray transient absorption spectroscopy," *J. Phys. Chem. Lett.* **2**, 628–632 (2011).
- ⁶⁴W. Gawelda, M. Johnson, F. M. de Groot, R. Abela, C. Bressler, and M. Chergui, "Electronic and molecular structure of photoexcited [Ru^{II}(bpy)₃]²⁺ probed by picosecond x-ray absorption spectroscopy," *J. Am. Chem. Soc.* **128**, 5001–5009 (2006).
- ⁶⁵J. Vinson, J. Rehr, J. Kas, and E. Shirley, "Bethe-Salpeter equation calculations of core excitation spectra," *Phys. Rev. B* **83**, 115106 (2011).
- ⁶⁶F. Neese, "The orca program system," *Wiley Interdiscip. Rev.: Comput. Mol. Sci.* **2**, 73–78 (2012).
- ⁶⁷C. Booth, Y. Jiang, D. Wang, J. Mitchell, P. Tobash, E. Bauer, M. Wall, P. Allen, D. Sokaras, D. Nordlund *et al.*, "Multiconfigurational nature of 5f orbitals in uranium and plutonium intermetallics," *Proc. Natl. Acad. Sci. U. S. A.* **109**, 10205–10209 (2012).
- ⁶⁸C. H. Booth, S. Medling, Y. Jiang, E. Bauer, P. Tobash, J. Mitchell, D. Veirs, M. Wall, P. Allen, J. Kas *et al.*, "Delocalization and occupancy effects of 5f orbitals in plutonium intermetallics using l3-edge resonant x-ray emission spectroscopy," *J. Electron Spectrosc. Relat. Phenom.* **194**, 57–65 (2014).
- ⁶⁹J. Tobin, S. Nowak, C. Booth, E. Bauer, S.-W. Yu, R. Alonso-Mori, T. Kroll, D. Nordlund, T.-C. Weng, and D. Sokaras, "Separate measurement of the 5f_{5/2} and 5f_{7/2} unoccupied density of states of UO₂," *J. Electron Spectrosc. Relat. Phenom.* **232**, 100–104 (2019).
- ⁷⁰K. O. Kvashnina, S. M. Butorin, P. Martin, and P. Glatzel, "Chemical state of complex uranium oxides," *Phys. Rev. Lett.* **111**, 253002 (2013).
- ⁷¹T. Vitova, I. Pidchenko, D. Fellhauer, P. Bagus, Y. Joly, T. Pruessmann, S. Bahl, E. Gonzalez-Robles, J. Rothe, M. Altmaier *et al.*, "The role of the 5f valence orbitals of early actinides in chemical bonding," *Nat. Commun.* **8**, 16053 (2017).
- ⁷²R. W. Schoenlein, "New science opportunities enabled by LCLS-II x-ray lasers," Technical Report No. SLAC-R-1053, SLAC, 2015.
- ⁷³C. J. Milne, P. Beaud, Y. Deng, C. Erny, R. Follath, U. Flechsig, C. P. Hauri, G. Ingold, P. Juranic, G. Knopp, H. Lemke, B. Pedrini, P. Radi, and L. Patthey, "Opportunities for chemistry at the SwissFEL X-ray Free Electron Laser," *Chimia* **71**, 299–307 (2017).